Research Article | Vol. 28, No. 23 / 9 November 2020 / Optics Express 34201
Optics EXPRESS

Design of continuously variant metasurfaces for conformal transformation optics

GIANLUCA RUFFATO[1,2,*] AND FILIPPO ROMANATO[1,2,3]

[1]L.i.f.e.L.a.b. Program, Consorzio per la Ricerca Sanitaria (CORIS), Veneto Region, Via Giustiniani 2, 35128, Padova, Italy
[2]Department of Physics and Astronomy 'G. Galilei', University of Padova, via Marzolo 8, 35131 Padova, Italy
[3]CNR-INFM TASC IOM National Laboratory, S.S. 14 Km 163.5, Basovizza, 34012 Trieste, Italy
*gianluca.ruffato@unipd.it

Abstract: Metasurfaces optics and structured light represent two emerging paradigms which are revolutionizing optics in a wide range of fields, from imaging to telecommunications, both in the classical and single-photon regimes. In this work, we present and describe a method for the design of high-resolution geometric-phase metasurfaces in the form of continuously variant sub-wavelength gratings, and we demonstrate how this technique is suitable for harmonic phase masks implementing conformal optical transformations. In this framework, we revisit the metasurface design of blazed gratings and spiral phase plates, the so-called *q*-plates, and we extend the method to the metasurface implementation of two conformal mappings, the *log-pol* and the circular-sector transformation, which have been exploited successfully to perform the generation, sorting and manipulation of structured light beams carrying orbital angular momentum.

1. Introduction

Metasurfaces represent nowadays one of the most rapidly expanding frontiers of nanophotonics, priding itself to revolutionize optics as we know it by displacing common optical elements in many large-scale applications and combining entirely altogether new functionalities [1]. Unlike diffractive and refractive elements, in which the phase shaping is introduced through a 3D control of the optical path difference, in metasurfaces the phase manipulation is imparted by structuring the medium at the sub-wavelength scale in order to artificially induce inhomogeneity and anisotropy. In Pancharatnam-Berry optical elements, for instance, a spatially-variant form-birefringence is exploited to impart a geometric phase which is equal to twice the local fast-axis angle [2]. After an initial implementation using plasmonic effects of metal gratings or resonant nano-antennas, metasurfaces based on high-index dielectric materials, e.g. titanium oxide or silicon, gained momentum due to their lower or negligible intrinsic losses and to the compatibility with standard industrial processes [3]. As a matter of fact, the possibility to etch a 2D binary pattern paves the way to the well-established fabrication techniques of semiconductor manufacturing, promoting metasurfaces as the merging point between lens making and silicon photonics.

Dielectric metasurfaces have been successfully demonstrated for beam steering and collimation [4,5], computer-generated holography [6] and imaging [7], showing the possibility to enclose in their thin 2D pattern more optical operations than the diffractive counterparts, such as polarization selectivity and aberration corrections [8]. Furthermore, the metasurface paradigm has recently accessed the flourishing field of structured light beams, providing a new tool for the realization of orbital angular momentum (OAM) [9] generators, the so-called *q*-plates [10–12], and the implementation of demultiplexers [13] for the sorting of total angular momentum, i.e. spin and OAM. Concurrently, the same tasks have been performed using custom-made liquid-crystal devices [14,15], exploiting the anisotropy of the photo-aligned polymers as geometric-phase

#400627 https://doi.org/10.1364/OE.400627
Journal © 2020 Received 18 Jun 2020; revised 31 Aug 2020; accepted 23 Sep 2020; published 27 Oct 2020

Optics EXPRESS

elements, however with a resolution which is dramatically affected by the diffraction-limited lithographic process.

High-index metasurfaces are commonly built up by assembling an aperiodic pattern of resonant digital sub-units, the so-called meta-atoms [16]. By acting on their geometrical features, such as shape, period, size and orientation, it is possible to control point-by-point the phase retardation of the transmitted wave and therefore induce a spatially-variant phase shaping. However, the resolution of the phase pattern is limited to the size of the single resonant cell, and the coupling between adjacent meta-atoms can introduce deviations from the ideal optical response. In this work, we consider the method based on continuously-variant sub-wavelength gratings for the design of effective-medium high-resolution metasurfaces based on the Pancharatnam-Berry phase. The local anisotropy is induced by properly engineering the sub-wavelength pattern in order to realize a spatially-variant wave plate, whose local fast axis is properly oriented on the plane according to the Pancharatnam-Berry phase which is required to impart the desired phase map. With respect to the meta-atoms technique, the continuity of the fast-axis rotation allows one to achieve a higher resolution in the spatially-variant manipulation of the input phasefront. This method, which was firstly introduced by Hasman's group for beam steering [17] and mode conversion [18], and lately demonstrated for angular momentum sorting [13], is here generalized to all the optical operations which are ascribable to a conformal mapping and implemented by harmonic phase plates. In general, conformal transformations allow to map efficiently the input beam to a desired output distribution of intensity and phase [19]. Here, we focus on the conformal mappings that have been implemented successfully to realize the basic optical operations on OAM, in particular the *log-pol* mapping [20], exploited for multiplexing and sorting [20–25], and the circular-sector transformation [26], used in OAM multiplication and division [26,27]. The former performs a mapping of the azimuthal coordinate over a linear direction, imparting an

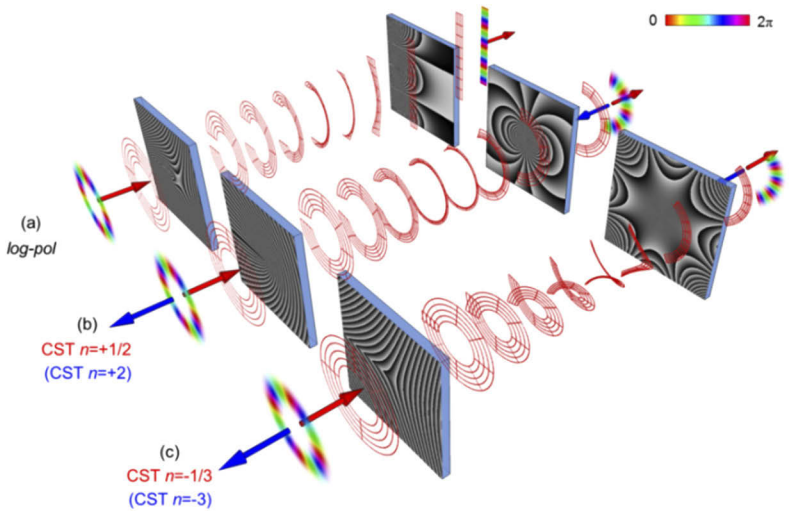

Fig. 1. Schemes of conformal transformations of an input OAM beam carrying an azimuthal phase $exp(i\ell\theta)$, with ℓ=+4. (a) *log-pol* mapping: the input azimuthal phase is mapped over a linear phase gradient by means of two confocal phase elements (unwrapper and phase-corrector). (b-c) Circular-sector transformation (CST): the input phase is mapped over a circular sector with amplitude $2\pi n$, with n=+1/2 (b) and n=-1/3 (c). The same setups perform the inverse circular-sector transformations when exploited in reverse (blue arrows direction), i.e. n=+2 (b) and n=-3 (c). In the depicted phase elements, the lens terms have been omitted in order to highlight the main contribution imparting the desired optical transformation.

Optics EXPRESS

unwrapping of the input phase onto a linear phase gradient [Fig. 1(a)]. The latter maps the whole azimuthal phase over a circular-sector, possibly including a sign inversion [Figs. 1(b),1(c)]. In each case, the optical operation is realized by a setup made of two confocal optical elements, in which the second element performs the inverse transformation when the same configuration is illuminated in reverse.

After describing the theory underlying the conversion of a harmonic phase function into its metasurface counterpart defined by a continuously-variant form birefringence, we apply this scheme to the different optical elements of interest in the field of structured light. In addition to the abovementioned mappings, we extend the analysis to more simple operations as those performed by blaze gratings and spiral phase plates, which can be included in the wider framework of harmonic phase elements. For each considered example, the phase map of the desired optical element is converted into a continuously-variant digital pattern of sub-wavelength gratings, whose period changes continuously between a minimum and a maximum value, imposed by the lithographic limitations and by the selected materials.

2. Continuously variant metasurfaces

The local anisotropy of a geometric-phase element is induced by properly engineering its sub-wavelength structure in order to create a spatially-variant wave plate, whose local extraordinary axis is properly oriented on the metasurface plane. By indicating with δ the phase difference between the ordinary (slow) and extraordinary (fast) axes, the optical response of a metasurface optical element $M(x, y)$ in the circular polarization basis $\boldsymbol{e}_{R/L} = [\ 1 \quad \pm i\ ]/\sqrt{2}$ is described as:

$$M(x,y)\cdot\boldsymbol{e}_{R/L} = \cos\left(\frac{\delta}{2}\right)\boldsymbol{e}_{R/L} - i\sin\left(\frac{\delta}{2}\right)e^{\pm 2i\vartheta(x,y)}\boldsymbol{e}_{L/R} \tag{1}$$

where $\vartheta(x, y)$ is the angle formed by the fast axis. Thus, the output beam includes two contributions. The first zero-order co-polarized term is proportional to $\cos(\delta/2)$ and can be eliminated by tuning the grating profile in order to set $\delta = \pi$. The second contribution is an orthogonally-polarized term carrying a phase modulation equal to twice the anisotropy angle, with sign depending on the input polarization. Therefore, in order to efficiently achieve the transfer of a desired phase pattern $\Omega(x, y)$, the metasurface should implement a spatially-variant half-wave plate with extraordinary axis orientation $\vartheta(x, y) = \Omega(x, y)/2$.

Among all the possible solutions to design the basic sub-wavelength unit, we focus on the approach based on introducing a sub-wavelength periodicity in the fast-axis direction [28]. As a matter of fact the effective refractive index is lower along the grating-vector direction, then its orientation can be exploited to control the transferred geometric phase [29]. In order to define the phase pattern with the highest lateral resolution, the orientation of the grating vector should vary continuously, defining a spatially-variant grating structure (Fig. 2). The continuity of the grating pattern is expressed by the following condition on the grating vector [17]:

$$\nabla \times \boldsymbol{K} = 0, \tag{2}$$

where the grating vector is spatially variant and defined as [Fig. 2(b)]:

$$\boldsymbol{K}(x,y) = K(x,y)[\ \cos\vartheta(x,y),\quad \sin\vartheta(x,y)\ ], \tag{3}$$

$\vartheta(x, y)$ being the local rotation angle, equal to half the geometric phase $\Omega(x, y)$. The curl should be intended on the 3D vector field (K_x, K_y, 0) confined to the metasurface plane, and we consider the nullification of the z-component, i.e. $\partial_x K_y$ - $\partial_y K_x = 0$, which represents the analytical condition for the vector $\boldsymbol{K}$ continuity on the plane. After substituting the grating-vector

Optics EXPRESS

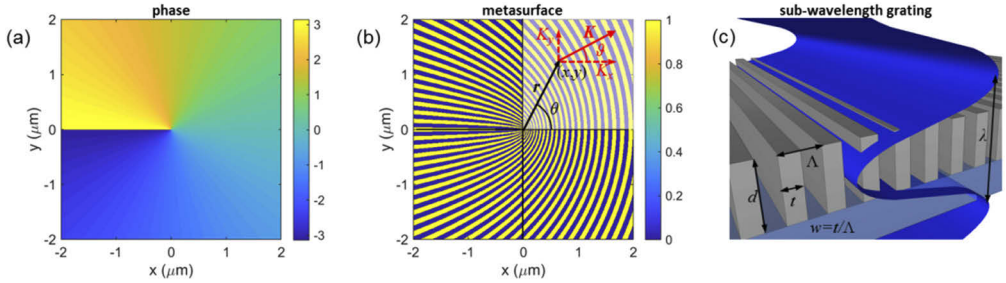

Fig. 2. Scheme of metasurface design in the form of sub-wavelength gratings. The phase pattern Ω of the optical element (a) is converted into a 2D structure (b) of continuously-variant gratings with sub-wavelength period (c). The local grating-vector angle $\vartheta(x, y)$ in (b) is equal to half the corresponding phase in (a). (c) Scheme of the digital grating pattern: period Λ and width t, duty-cycle $w = t/\Lambda$, thickness d, incident wavelength λ.

components as expressed in Eq. (3), we obtain the following conditions on the grating-vector partial derivatives:

$$\frac{\partial K}{\partial x} = -\frac{K}{2}\frac{\partial \Omega}{\partial y}, \quad \frac{\partial K}{\partial y} = \frac{K}{2}\frac{\partial \Omega}{\partial x}, \tag{4}$$

where we used the relation $\vartheta(x, y) = \Omega(x, y)/2$. The previous couple of equations can be rewritten in the compact form:

$$\nabla \ln K = \frac{1}{2} R_{\pi/2} \nabla \Omega, \tag{5}$$

where $R_{\pi/2}$ is the 2×2 matrix describing a $\pi/2$ counter-clockwise rotation on the (x, y) plane:

$$R_{\pi/2} = \begin{bmatrix} 0 & -1 \\ 1 & 0 \end{bmatrix}. \tag{6}$$

Equation (5) has two important implications. From a geometrical point of view, it expresses the local orthogonality between the gradient of the phase function Ω and the gradient of the grating modulus K, since $\ln(\cdot)$ is a monotonic function. Therefore, at each point of coordinates (x, y), the line of equal phase $\overline{\Omega} = \Omega(x, y)$ is expected to be perpendicular to the local isoline of the function $K(x, y)$. Secondly, Eq. (5) implies a strict condition on the phase function Ω. As a matter of fact, by acting on the both sides of Eq. (5) with the inverse rotation matrix $R_{-\pi/2}$, performing a $\pi/2$ clockwise rotation, and applying the divergence operator $\nabla\cdot$, we obtain the following condition on Ω:

$$\nabla^2 \Omega = 0, \tag{7}$$

which implies that the phase function Ω must be harmonic. As recently demonstrated in [30], a particularly interesting family of harmonic phase functions is represented by those implementing an anti-holomorphic conformal mapping $g(\bar{z}) = u(x, y) + iv(x, y)$ on the complex plane, where $z = x + iy$. The real and imaginary parts define an optical transformation mapping a point (x, y) on the input plane to a point of coordinates $(u(x, y), v(x, y))$ on the destination plane. In the complex function theory, an anti-holomorphic function satisfies the following identity on the Wirtinger

Optics EXPRESS

operator:

$$\frac{\partial g}{\partial z} = \frac{1}{2}\left(\frac{\partial}{\partial x} - i\frac{\partial}{\partial y}\right) g = 0, \tag{8}$$

which is equivalent the following Cauchy-Riemann conditions on the functions u and v, i.e. on the real and imaginary parts of g, respectively:

$$\frac{\partial u}{\partial x} = -\frac{\partial v}{\partial y}, \quad \frac{\partial u}{\partial y} = \frac{\partial v}{\partial x}. \tag{9}$$

In the stationary phase approximation [19], the new coordinates (u, v) of the point (x, y) after the new mapping on the plane at a distance f, can be implemented by means of an optical element whose phase function $\Omega(x, y)$ satisfies the following relation:

$$\nabla\Omega = \frac{k}{f}[\ u \quad v\ ] = \frac{k}{f}[\ \Re\{g\} \quad \Im\{g\}\ ], \tag{10}$$

being $k = 2\pi/\lambda$ the wavevector. After taking the divergence of the gradient of Ω in Eq. (10) and using the relations in Eq. (9), then the harmonic condition expressed in Eq. (7) is obtained. Details on the derivation of Eq. (10) in the paraxial regime are reported in the Supplemental document.

The combination of Eq. (5) with Eq. (10) leads to the following relation between the grating vector K and the components of the conformal transformation g:

$$\nabla \ln K = \frac{k}{2f} R_{\pi/2}[\ \Re\{g\} \quad \Im\{g\}\ ] = \frac{k}{2f}[\ \Re\{ig\} \quad \Im\{ig\}\ ], \tag{11}$$

where we used the result that a $\pi/2$ rotation corresponds to the multiplication by a factor i on the complex plane. Equation (11) provides the analytical tool to calculate the grating-vector function $K(x, y)$ for the given phase Ω implementing the conformal mapping g.

Once the grating vector $K(x, y)$ is determined, the whole metasurface structure can be outlined by introducing the grating potential $\psi(x, y)$, whose existence is assured by the conservative condition on the grating vector [Eq. (2)], calculated by integration over an arbitrary path:

$$\nabla\psi = \boldsymbol{K}. \tag{12}$$

Finally, the digitalization of the grating potential is performed by imposing the following period-dependent Lee-type condition:

$$T(x, y) = \Theta\{\cos\psi(x, y) - \cos(\pi w(\Lambda(x, y)))\}, \tag{13}$$

where Θ is the Heaviside function, $w(\Lambda(x, y))$ is the duty-cycle $w(\cdot)$ calculated for the grating period Λ at the position (x, y): $\Lambda(x, y) = 2\pi/K(x, y)$[Figs. 2(b),2(c)]. As a matter of fact, the spatial dependency of the grating modulus $K(x, y)$ implies necessarily a variation of the grating period $\Lambda(x, y)$, and a consequent change of the effective refractive indices and of the resulting phase difference δ, unless the duty-cycle is tuned accordingly. Therefore, in order to maintain a uniform $\delta=\pi$ over the whole pattern, despite the change in the grating period, the solution is to introduce a spatially-variant duty-cycle $w(\Lambda(x, y))$, as done in Eq. (13). However, the grating period is not allowed to vary unconditionally. Its value should not exceed a maximum threshold, given by the cut-off wavelength, beyond which the sub-wavelength regime could be violated, and should not go below a minimum value which could be barely affordable by the fabrication process. For this reason, the metasurface pattern requires the fragmentation over complementary zones where the period is allowed to vary continuously between an upper limit Λ_M and a lower limit Λ_m, depending on the working wavelength, on the metasurface material, and on the maximum

Optics EXPRESS

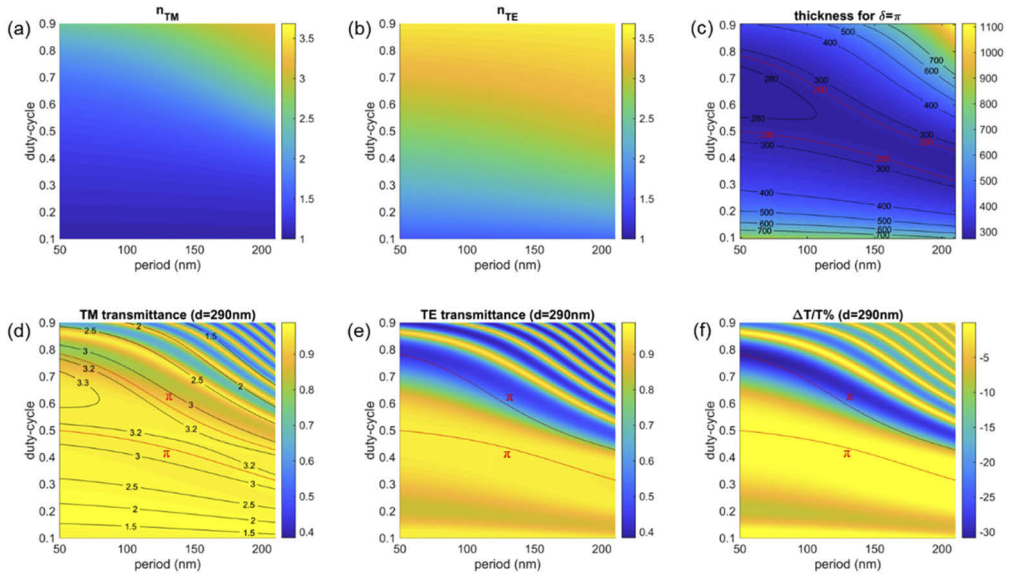

Fig. 3. Rigorous coupled-wave analysis (RCWA) of a silicon sub-wavelength grating in air for normal incidence at λ=780 nm (n_{Si}=3.684), glass substrate. Effective refractive indices n_{TE} and n_{TM} for TM- (a) and TE- (b) polarization as a function of the grating period and duty-cycle. (c) Grating thickness [nm] providing half-wave delay (δ=π) between TE and TM polarization and corresponding TE- (d) and TM- (e) polarization transmittance. In (d) the contour plot highlights the configurations of equal phase retardation δ [rad]. (f) Transmittance variation $\Delta T/T\% = 2(T_{TE}-T_{TM})/(T_{TE}+T_{TM})\cdot 100$. Red solid curves in (d-f): half-wave plate configurations (δ=π) for the selected thickness of 290 nm.

aspect ratio achievable with the selected fabrication protocol. At the boundaries between different zones, where a discontinuity occurs in the grating period, the grating orientation will be the same, guaranteeing the continuity of the transferred geometric phase.

For given wavelength and metasurface material, numerical simulations must be performed in order to calculate the effective refractive indices n_{TE} and n_{TM}, and extract the optimal configurations of period and duty-cycle satisfying the condition $\delta=\pi$ for the selected thickness of the digital pattern. We considered TM- and TE-polarizations parallel and orthogonal to the grating-vector direction, i.e. the fast-axis direction, respectively. To this aim, numerical simulations have been performed implementing Rigorous Coupled-Wave Analysis (RCWA) [31–33] for a binary silicon grating in air at 780 nm deposited over a glass substrate, in order to infer the optimal design. These results are summarized in Fig. 3. In Fig. 3(a) and 3(b), the effective indices n_{TE} and n_{TM} are shown as a function of the grating period and duty-cycle. For the same configurations, the corresponding grating thickness satisfying the condition $\delta=\pi$ is reported in Fig. 3(c). As shown in Fig. 3(c), for given grating thickness and period, two values of duty-cycle can exist providing π-phase difference. Then, for a selected grating thickness, two distinct optimal branches exist of duty-cycle values as a function of the grating period, as shown for the value of 290 nm. As shown in Fig. 3(d) and 3(e), the two π-branches are not equivalent in terms of transmittance. While the lower branch has substantially the same transmittance for TE and TM polarization, the upper branch exhibits a different behavior [Fig. 3(f)]. For this reason, in the following calculations we will consider the lower branch for the design of continuously-variant metasurfaces of sub-wavelength gratings in silicon with thickness d of 290 nm, designed for the specific wavelength of 780 nm. Under the previous assumptions, the theoretical conversion efficiency at the design wavelength is equal to one. However, the overall transmission will be

Optics EXPRESS

lower, due to the reflection at the grating/air and grating/substrate interfaces, and around 93%, as shown in Figs. 3(d) and 3(e) (silicon absorption is around 3%).

3. Application to conformal transformation optics

In the following sections, the theory outlined above will be applied to several cases of interest in the field of structured light generation and manipulation with conformal transformation optics. In the specific, we will show the design of continuously-variant metasurfaces of sub-wavelength gratings implementing harmonic phase functions corresponding to several optical operations: blazed grating, spiral phase plate, *log-pol* transformer, circular-sector transformer.

3.1. Blazed grating

The general phase profile of a blazed grating of period Λ_G forming an angle ϕ with the x-axis is given by:

$$\Omega(x, y) = \alpha x + \beta y, \tag{14}$$

where $\gamma = \sqrt{\alpha^2 + \beta^2} = 2\pi/\Lambda_G$, $\phi = \arctan(\beta/\alpha)$. The linear phase profile in Eq. (14) is a trivial solution of Laplace's Eq. (7) in Cartesian coordinates, and according to the relation in Eq. (10) it corresponds to the constant complex function:

$$g(\bar{z}) = \frac{f}{k}(\alpha + i\beta). \tag{15}$$

Then, after introducing the last definition into Eq. (11), we obtain the following equation for the grating vector K unknown:

$$\nabla \ln K = \frac{1}{2}[\ -\beta \quad \alpha\ ], \tag{16}$$

which provides the following solution:

$$K(x, y) = K_0 \exp\left(-\frac{\beta}{2}x + \frac{\alpha}{2}y\right), \tag{17}$$

being K_0=2π/Λ_0 the grating vector in (x, y)=(0, 0). The grating potential, defined in Eq. (12), can be calculated analytically and its value is given by:

$$\psi(x, y) = \frac{2K_0}{\gamma} \exp\left(-\frac{\beta}{2}x + \frac{\alpha}{2}y\right) \sin\left(\frac{\alpha}{2}x + \frac{\beta}{2}y - \phi\right). \tag{18}$$

Therefore, by applying the digitalization algorithm in Eq. (13), the metasurface binary pattern can be obtained. However, as discussed in the previous section, it is fundamental to limit the grating period between two values Λ_M and Λ_m. In the reference frame (x', y'), rotated of ϕ with respect to (x, y), the grating period varies monotonically in the y' direction according to $\Lambda(y')=\Lambda_0 \cdot \exp(-\gamma y'/2)$. As a consequence, the metasurface should be divided into complementary stripes, defined within $y'=jL$ and $y'=(j+1)L$, with j integer, and L given by

$$L = \frac{2}{\gamma} \ln\left(\frac{\Lambda_M}{\Lambda_m}\right). \tag{19}$$

Inside the jth stripe, the digitalization is performed on the potential in Eq. (18) defined in the new reference frame:

$$\psi_j(x', y') = \frac{4\pi}{\gamma\Lambda_m} \exp\left(\frac{\gamma}{2}(y' - jL)\right) \sin\left(\frac{\gamma}{2}x' - \phi\right). \tag{20}$$

In Fig. 4, the conversion of a blazed grating into a spatially-variant sub-wavelength digital grating is shown, for γ=0.4 μm^{-1}, ϕ=π/6. The pattern is discretized into meta-stripes according

Optics EXPRESS

to Eq. (19). Inside each meta-stripe, the grating period is allowed to vary between an upper limit Λ_M=0.250 μm, and a lower limit Λ_m=0.050 μm. It is worth noting the continuity of the grating angle at the boundaries between different stripes. The duty-cycle of the final metasurface pattern changes as a function of the grating period in order to guarantee a uniform π-delay between TE and TM polarizations, following the lower branch in Fig. 3(d) for d=290 nm.

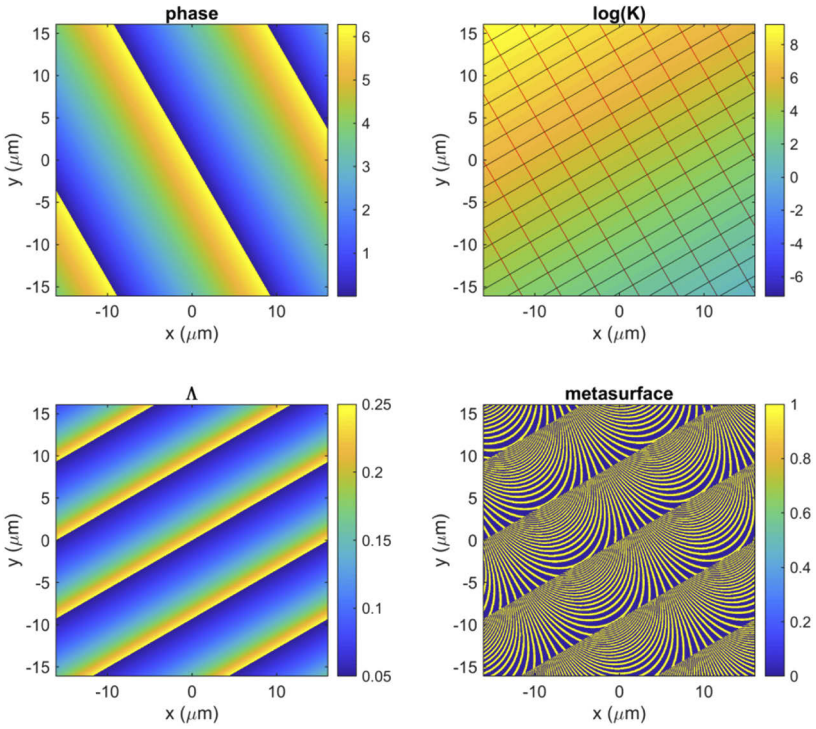

Fig. 4. Conversion of a blazed grating phase map (a) into a continuously-variant sub-wavelength digital grating (d). (a) Phase map of a selected zone of the blazed grating phase pattern. γ=0.4 μm^{-1}, ϕ=π/6. (b) Grating vector (logarithmic scale) of the selected zone. Black and red lines refer to $log(K)$ and phase isolines, respectively. (c) Period Λ [μm] of the sub-wavelength grating over the selected zone. The zone is discretized into meta-stripes according to Eq. (19). Inside each meta-stripe, the grating period can vary between an upper limit, close to the structural cut-off, and a lower limit imposed by the fabrication process. (d) After imposing a period-dependent Lee-type digitalization [Eq. (13)], the sub-wavelength binary metasurface is finally obtained. The duty-cycle changes as a function of the grating period according to Fig. 3 (grating thickness 290 nm).

3.2. *Spiral phase plate (q-plate)*

A spiral phase plate is characterized by a stair-case phase profile as [34]:

$$\Omega(r, \theta) = \ell\theta, \tag{21}$$

where ℓ, in units of the reduced Planck constant, is the amount of orbital angular momentum (OAM) per photon transferred to the impinging beam (Fig. S1 in the supplemental document). The azimuthal phase profile is a trivial solution of Laplace's Eq. (7) in polar coordinates, and

Optics EXPRESS

according to Eq. (10) it corresponds to the conformal mapping:

$$g(\bar{z}) = \frac{f\ell}{k}\frac{i}{\bar{z}} = \frac{f\ell}{k}\frac{i\cos\theta - \sin\theta}{r}. \tag{22}$$

After introducing the last relation into Eq. (11), we obtain the following equation for the grating-vector modulus K unknown:

$$\nabla \ln K = -\frac{\ell}{2}\left[\frac{\cos\theta}{r}\frac{\sin\theta}{r}\right], \tag{23}$$

which provides the following solution:

$$K(x,y) = K_0\left(\frac{r}{r_0}\right)^{-\frac{\ell}{2}}, \tag{24}$$

being K_0=2π/Λ_0 the grating vector modulus in $r = r_0$. As in the previous case the grating potential can be calculated analytically, and it is given by:

$$\psi(r,\theta) = K_0 r_0\left(\frac{r}{r_0}\right)^{1-\frac{\ell}{2}}\frac{\cos\left(\left(1-\frac{\ell}{2}\right)\theta\right)}{1-\frac{\ell}{2}}. \tag{25}$$

As expressed by Eq. (24), the modulus of the grating vector varies monotonically in the radial direction. Then, it is convenient to calculate the metasurface over complementary concentric annuli, defined within r_j and r_{j+1}, being j integer and positive, given by:

$$r_{j+1} = r_j\left(\frac{\Lambda_M}{\Lambda_m}\right)^{\frac{2}{\ell}}. \tag{26}$$

Inside each zone, the potential is defined as in Eq. (25), with the definitions r_0=r_j and K_0=2π/Λ_m or K_0=2π/Λ_M, for positive or negative values of ℓ, respectively. For positive ℓ, the grating period increases with the radial coordinate, from the minimum value Λ_m at $r = r_j$ to the maximum value Λ_M at $r = r_{j+1}$. Conversely, for negative ℓ, the grating period decreases from the maximum value Λ_M at $r = r_j$ to the minimum value Λ_m at $r = r_{j+1}$. This is shown in Fig. 5 and Fig. 7, for ℓ=+1 and ℓ=-1, respectively. The resulting metasurface represents the sub-wavelength grating implementation of a q-plate, with $q = \ell/2$ (Fig. 6 and Fig. 8). In Fig. 9, different continuously-variant q-plates are shown, for q-values in the set {+1.5, +2, -1, -1.5}.

3.3. Log-pol transformation

The *log-pol* mapping is an efficient method for OAM demultiplexing purposes, since it realizes a unitary correspondence between angular momentum and linear momentum states which can be easily separated by means of a Fourier lens [Fig. 1(a)] [20]. This transformation maps the azimuthal coordinate θ=*arctan*(y/x) to the Cartesian coordinate v, unwrapping the input OAM beam onto a linear intensity distribution with length $2\pi a$ on the plane (u, v) (Fig. S2 in the supplemental document). In the complex formalism, the *log-pol* mapping is described by the anti-holomorphic function $g(\bar{z}) = u + iv$ given by:

$$g(\bar{z}) = -a\ln\left(\frac{\bar{z}}{b}\right) = -a\ln\frac{r}{b} + ia\theta, \tag{27}$$

where a and b are arbitrary parameters, controlling the size and position of the unwrapped azimuthal phase. A second element, the so-called phase-corrector, is needed to restore the linear

Optics EXPRESS

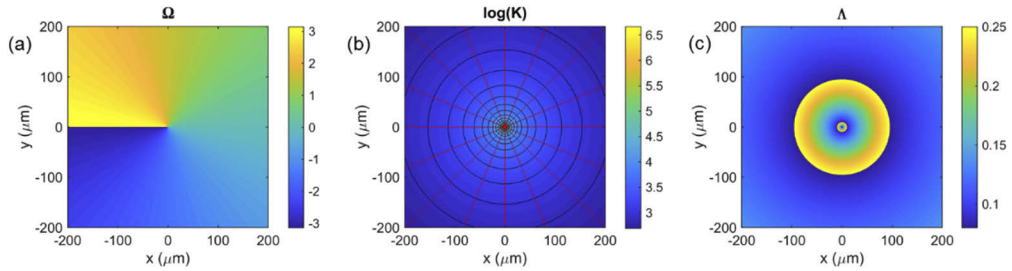

Fig. 5. (a) Phase map Ω of a spiral phase plate with ℓ=+1. (b) Corresponding sub-wavelength grating vector (logarithmic scale). Black and red lines refer to $log(K)$ and phase isolines, respectively. (c) Period Λ [μm] of the sub-wavelength grating over the selected area. The area is discretized into complementary concentric annuli according to Eq. (26). Inside each zone, the grating period varies between a lower and an upper threshold.

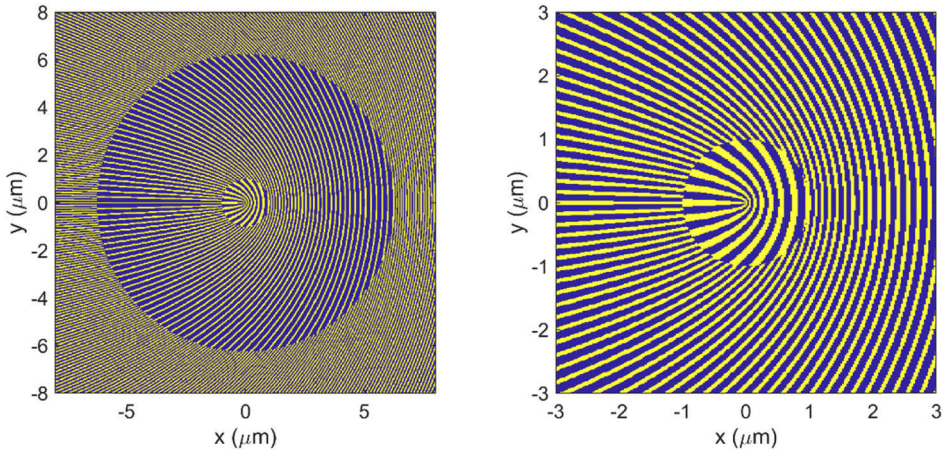

Fig. 6. Continuously-variant sub-wavelength grating metasurface implementing the spiral phase plate in Fig. 5(a). The metasurface implements a q-plate with q=+0.5. On the right: detail of the central phase singularity.

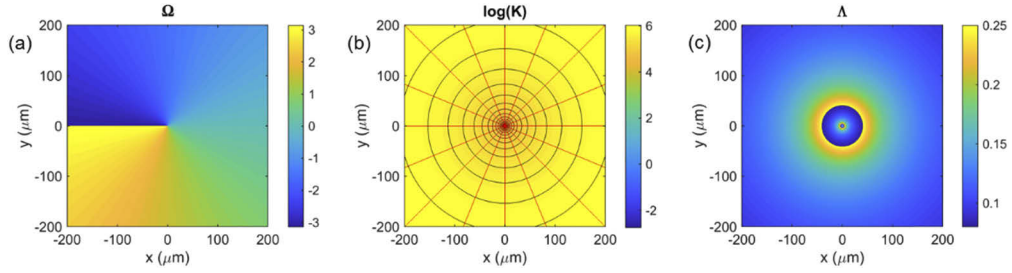

Fig. 7. (a) Phase map Ω of a spiral phase plate with ℓ=-1. (b) Sub-wavelength grating vector (logarithmic scale). Black and red lines refer to $log(K)$ and phase isolines, respectively. (c) Period Λ [μm] of the sub-wavelength grating over the selected area. The area is discretized into complementary concentric annuli according to Eq. (26). Inside each zone, the grating period varies between a lower and an upper threshold.

Optics EXPRESS

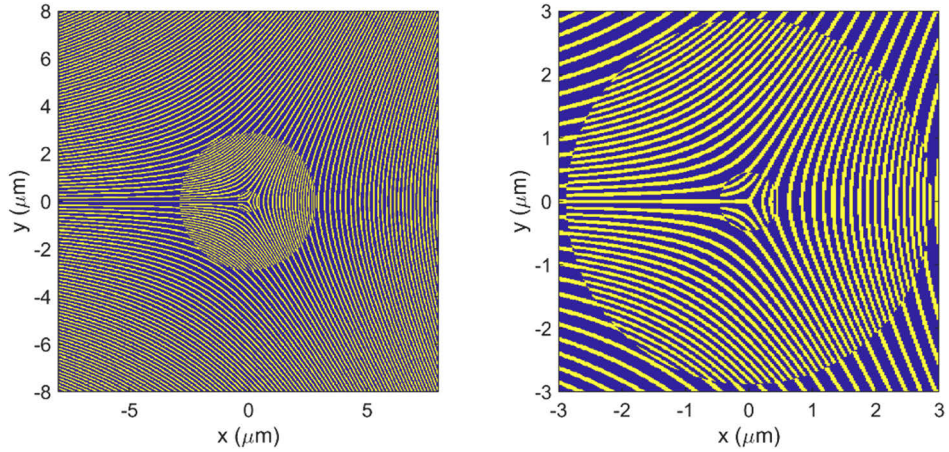

Fig. 8. Continuously-variant sub-wavelength grating metasurface implementing the spiral phase plate in Fig. 7(a). The metasurface implements a q-plate with q=-0.5. On the right: detail of the central phase singularity.

phase gradient compensating for the different paths travelled by each point of the wavefront. In other words, it performs the inverse anti-holomorphic transformation $g^{-1}(\overline{q}) = x + iy$, where $q = u + iv$, when the sequence of the two elements is illuminated in reverse order [22]. After inverting the complex expression of Eq. (27) we obtain:

$$g^{-1}(\overline{q}) = be^{-\frac{\overline{q}}{a}} = be^{-\frac{u}{a}}\left(\cos\frac{v}{a} + i\sin\frac{v}{a}\right), \tag{28}$$

The integration of Eq. (10) provides the well-known harmonic phase functions implementing the conformal transformations given in Eqs. (27) and (28):

$$\Omega_{UW}(x,y) = \frac{2\pi a}{\lambda f}\left(y\arctan\frac{y}{x} - x\ln\frac{r}{b} + x\right), \tag{29}$$

$$\Omega_{PC}(u,v) = -\frac{2\pi ab}{\lambda f}\exp\left(-\frac{u}{a}\right)\cos\left(\frac{v}{a}\right), \tag{30}$$

corresponding to the unwrapper phase Ω_{UW} and to the phase-corrector phase Ω_{PC}, respectively.

After introducing the expressions in Eqs. (27) and (28) into Eq. (11), we obtain the following equations for the corresponding grating vectors unknown:

$$\nabla \ln K_{UW} = -\frac{ka}{2f}\left[\begin{array}{cc}\theta & \ln\left(\frac{r}{b}\right)\end{array}\right], \tag{31}$$

$$\nabla \ln K_{PC} = -\frac{kb}{2f}e^{-\frac{u}{a}}\left[\begin{array}{cc}-\sin\left(\frac{v}{a}\right) & \cos\left(\frac{v}{a}\right)\end{array}\right], \tag{32}$$

which provide the following solutions:

$$K_{UW}(x,y) = K_0\exp\left(\frac{\pi a}{\lambda f}\left(-x\arctan\frac{y}{x} - y\ln\frac{r}{b} + y\right)\right), \tag{33}$$

$$K_{PC}(u,v) = K_0\exp\left(\frac{\pi ab}{\lambda f}e^{-\frac{u}{a}}\sin\frac{v}{a}\right), \tag{34}$$

being K_0=2π/Λ_0 the grating vector in (x, y)=(0, 0). As shown in Eqs. (33) and (34) and in Fig. 10, the grating period exhibits a complicated pattern, and an analytical solution for the

Optics EXPRESS

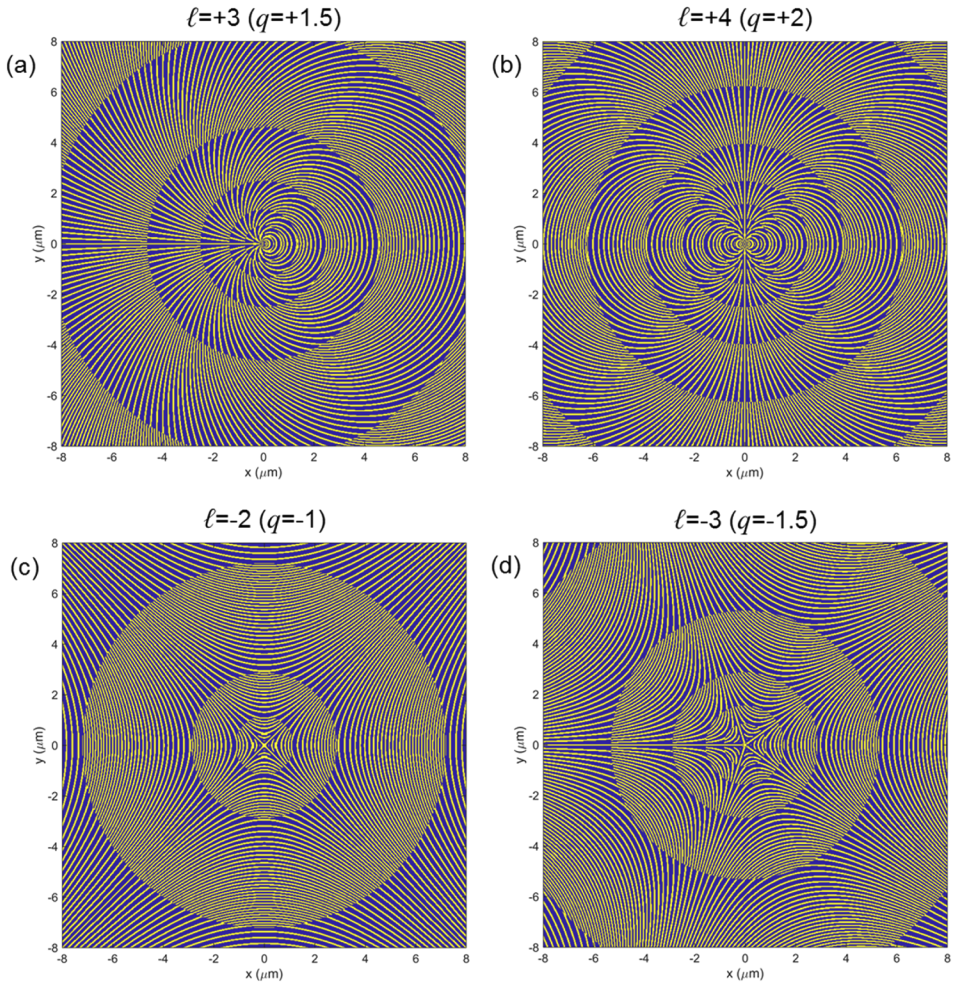

Fig. 9. Examples of continuously-variant sub-wavelength grating metasurfaces implementing q-plates for different values of the parameter q.

corresponding grating potential in Eq. (12) appears not to exist. Then, an alternative approach consists in discretizing the whole pattern into a mesh of meta-pixels, and in calculating the grating potential numerically inside each meta-pixel. Inside each zone, the grating period is bounded between the two threshold values Λ_m and Λ_M, as shown in Fig. 11, and the meta-pixel size is selected so that the grating period does not exceed the upper threshold. This can be done by calculating analytically the maximum value of grating period inside each area using the Eqs. (33) or (34) for a given meta-pixel size. If the maximum value is greater than the fixed threshold, then the meta-pixel size must be reduced, and the process is repeated until the condition is satisfied. At that point, the grating potential is calculated numerically. Finally, the digitalization process in Eq. (13) allows obtaining the metasurface pattern. At the boundaries between different meta-pixels, the grating-vector angle is continuous, therefore assuring the continuity of the transferred geometric phase.

Optics EXPRESS

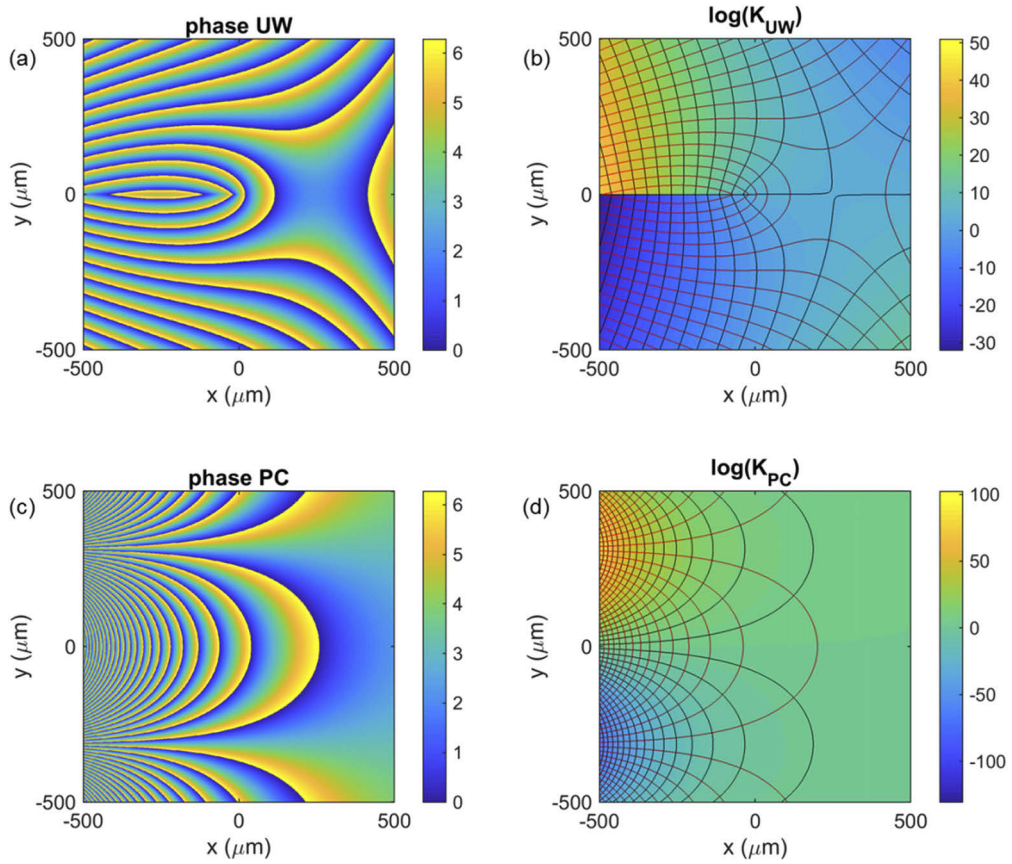

Fig. 10. Unwrapper (a) and phase-corrector (c) phase maps and corresponding grating vectors (logarithmic scale) (b, d). Black and red lines refer to $log(K)$ and phase isolines, respectively. Design parameters of the transformation: a=200 μm, b=250 μm, f=35 mm, λ=780 nm.

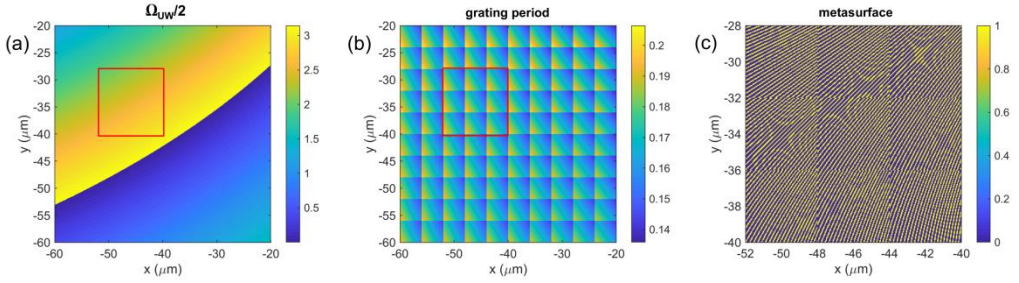

Fig. 11. (a) Ω/2 map of a selected zone of the un-wrapper phase pattern in Fig. 10(a). (b) Period [μm] of the sub-wavelength grating over the selected zone. The area is discretized into meta-pixels of lateral size 4 μm. Inside each meta-pixel, the grating period can vary between an upper limit, close to the structural cut-off, and a lower limit imposed by the fabrication process. (c) Continuously-variant sub-wavelength grating metasurface within the red marked area in (a) and (b).

Optics EXPRESS

3.4. Circular-sector transformation

An n-fold circular-sector transformation maps the azimuthal coordinate θ to the new value $n\theta$, performing a projection of the input phase to a circular sector with amplitude $2\pi n$ [26] [Figs. 1(b),1(c)] (Fig. S3 in the supplemental document). It is generated by the complex anti-holomorphic function

$$g(\bar{z}) = a\left(\frac{\bar{z}}{b}\right)^{-n} = a\left(\frac{r}{b}\right)^{-n}(\cos n\theta + i\sin n\theta). \tag{35}$$

where a and b are arbitrary scaling parameters acting on the radial coordinate. According to the relation in Eq. (10), the corresponding conformal transformation is implemented by the phase element:

$$\Omega_n(r,\theta) = \frac{2\pi ab}{\lambda f}\left(\frac{r}{b}\right)^{1-n}\frac{\cos((1-n)\theta)}{1-n}, \tag{36}$$

This transformation has been recently demonstrated to represent the key element to perform multiplication and division of OAM [26,27]. As in the case of OAM sorting with *log-pol* mapping, a second element is necessary in order to perform a phase correction and retrieve the desired phase distribution. This second element actually performs the inverse transformation of Eq. (35) [Figs. 1(b),1(c)], then it is easily obtained under the substitutions $n \leftrightarrow 1/n$ and $a \leftrightarrow b$. Therefore, the functional dependence on the spatial coordinates remains unaltered. After introducing Eq. (36) into Eq. (11), we obtain the following equation for the grating vector modulus K unknown:

$$\nabla \ln K_n = \frac{ka}{2f}\left(\frac{r}{b}\right)^{-n}\begin{bmatrix} -\sin n\theta & \cos n\theta \end{bmatrix}, \tag{37}$$

which provides the following solution:

$$K_n(r,\theta) = K_0 \exp\left(-\frac{\pi ab}{\lambda f}\left(\frac{r}{b}\right)^{1-n}\frac{\sin((1-n)\theta)}{1-n}\right), \tag{38}$$

being K_0=2π/Λ_0 the grating-vector modulus in r=0. In Fig. 12, the circular-sector transformation phase and the corresponding grating-vector modulus are shown for different values of the parameter n. It is somehow surprising the analogy between the phase function in Eq. (36) and the q-plate grating potential in Eq. (25), under the correspondence $n \leftrightarrow q$ ($q = \ell/2$). This becomes evident after comparing the continuously-variant q-plates in Figs. 6,8 and 9, with the corresponding phase patterns of the circular-sector transformers in Fig. 12. In particular, it is worth considering the analogy between Fig. 6($\ell = +1$) and Fig. 12(e) ($n = +1/2$), between Fig. 8($\ell = -1$) and Fig. 12(g) ($n = -1/2$), and between Fig. 9(b)($\ell = +4$) and Fig. 12(a) ($n = +2$)

As shown in the previous section, the final metasurface pattern is obtained by calculating the grating potential numerically over a mesh of complementary meta-pixels, allowing the grating period to vary within a minimum and a maximum value. This is shown in Fig. 13 for a selected area of the circular-sector transformer in Fig. 12(d.1) for n=-3.

Optics EXPRESS

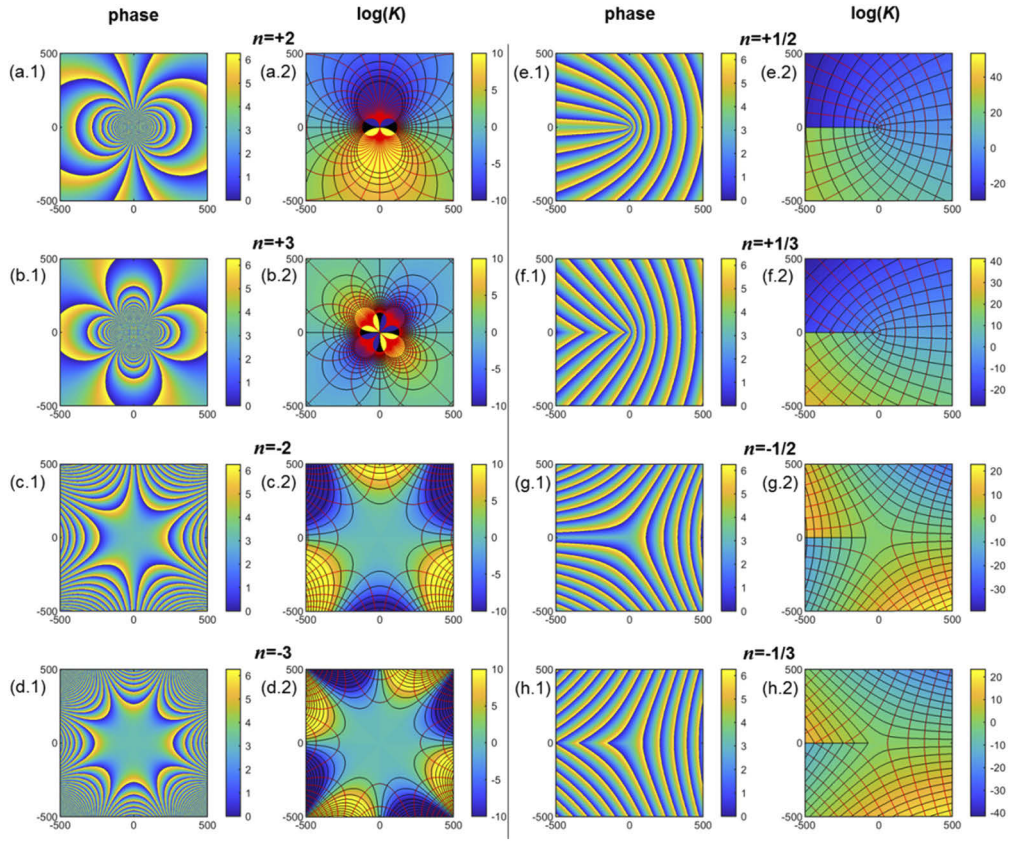

Fig. 12. Circular-sector transformer phase maps and corresponding grating vectors (logarithmic scale) for several values of n. Black and red lines refer to $log(K)$ and phase isolines, respectively. Design parameters: a=300 μm, b=300 μm, f=35 mm, λ=780 nm. Values on the x- and y-axis in microns.

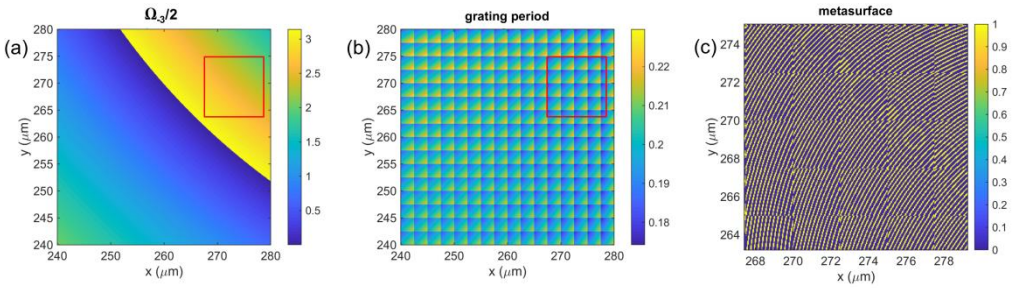

Fig. 13. (a) Ω/2 map of a selected zone of the circular-sector transformer in Fig. 12(d.1) (n=-3). (b) Period [μm] of the sub-wavelength grating over the selected zone. The zone is discretized into meta-pixels of lateral size 2.5 μm. Inside each meta-pixel, the grating period can vary between an upper limit, close to the structural cut-off, and a lower limit imposed by the fabrication process. (c) Continuously-variant sub-wavelength grating metasurface within the red marked area in (a) and (b).

Optics EXPRESS

4. Discussion

In this work, we described the implementation of high-resolution geometric-phase metasurfaces in the form of continuously-variant sub-wavelength gratings. The anisotropy of the medium is artificially induced by the form-birefringence of the grating pattern, and the local control of the fast-axis orientation, i.e. of the grating-vector angle, allows the desired shaping of the wavefront. With respect to other techniques, based on resonant plasmonic or dielectric anisotropic elements or optically-oriented liquid crystals, this technique can assure a higher resolution in the geometric phase definition, due to the continuity of the grating-vector rotation.

This approach is suitable to the metasurface implementation of phase functions that are harmonic, i.e. solutions of Laplace's equation. This family includes common optical elements such as blazed gratings and spiral phase plates, and extends to conformal transformation optics generated by anti-holomorphic mappings. In this framework, we applied this design tool for the metasurface implementation of two conformal mappings of crucial importance in the field of OAM manipulation: the *log-pol* mapping and the circular-sector transformation. For each mapping, we calculated the analytical expression of the grating vector modulus and we showed how to design the corresponding continuously-variant metasurface. The requirement of limiting the grating period within upper and lower values imposes the fragmentation of the phase pattern onto a set of complementary zones. Inside each area, the grating period and duty-cycle vary continuously in order to achieve the highest resolution and efficiency conversion, while the continuity of the grating-vector angle is assured at the boundaries between different zones.

With respect to diffractive optics, the metasurface paradigm allows to simplify the lithographic process and realize the sub-wavelength pattern with the highest adherence to the simulated design. As a matter of fact, a 3D surface-relief structure requires a high smoothness of the surface and, in particular, a sharp definition of 2π-phase jumps, in order not to introduce deviations from the exact profile which could promote a detrimental zero-order term. On the other hand, the continuously-variant effective anisotropy of the metasurface defines the geometric phase without discontinuities, by means of a 2D binary pattern. Deviations from the ideal profile, for instance due to a mismatch of the grating depth with the optimal one, affect the value of the phase delay δ and feed the presence of the co-polarized zero-order term. However, since that contribution is orthogonally polarized to the transmitted phase-shaped beam, as described in Eq. (1), it can be filtered out by using a quarter-wave plate and a polarizer in cascade. Moreover, this sequence allows extending the use of the metasurface also to wavelengths different from the design wavelength. As a matter of fact, the transferred phase has a geometric nature and is proportional to twice the local grating orientation, which is fixed for any input wavelength. Then, an input wavelength which is different from the optimal one will experience the same phase shaping, however with a lower conversion efficiency, given by $\sin^2(\delta/2)$. As mentioned beforehand, the zero-order contribution, proportional to $\cos^2(\delta/2)$, is orthogonally polarized with respect to the modulated term and can be filtered out by using an achromatic circular polarizer, i.e. the sequence of an achromatic quarter-wave plate and a linear polarizer. For a silicon metasurface on glass, with a thickness of 290 nm and designed for the wavelength of 780 nm, as those shown in the previous section, the conversion efficiency is expected to maintain higher than 95% in the range from 710 to 870 nm (Fig. S4 in the supplemental document).

It is always possible to exploit the handedness dependence of the optical response in order to integrate a circular-polarization splitting, by adding a tilt term to the whole phase. When two confocal elements in cascade are needed, e.g. for OAM manipulation with *log-pol* or circular-sector transformations, a piecewise design of the second element is required in order to consider the impinging of the two orthogonal polarizations onto different non-overlapping zones, as shown in [13,14]. Since the focusing term cannot be included in the metasurface, an additional lens is needed and the two elements must be placed at the front- and back-focal planes

Optics EXPRESS

of the lens [14]. A more compact solution consists in applying diffractive Fresnel contact-lenses directly on the two metasurfaces [13].

It is worth noting the unexpected analogy between the phase function of circular-sector transformations and the q-plate grating potential, under the correspondence $n \leftrightarrow q$. Since the phase function of the n-fold circular-sector transformation corresponds to the integrated potential of an electric or magnetic multipole of order m=1-n, as demonstrated in [30], this analogy suggests the possibility to engineer self-assembled liquid crystals q-plate using the driving field of properly oriented electrodes or magnets, as shown for instance in [35–37] for q-plates with q=+1. In this case, with respect to optically-oriented liquid crystals, the self-orientation of the liquid crystal molecules provides a far higher resolution in the q-plate definition, while the optimization for a specific wavelength can be obtained by tuning the applied external voltage.

5. Conclusions

To conclude, we provided a method for the design of continuously-variant metasurfaces of sub-wavelength grating which can be applied to realize high-resolution geometric-phase optical elements. In particular, we demonstrated how this tool can be exploited for the metasurface design of optical elements implementing the generation, manipulation and steering of OAM beams. The conversion of the optical element to a thin digital pattern represents a fundamental step forward the integration of optics and silicon photonics. As a matter of fact, this design enables the integration of optical devices directly into existing technology platforms, due to the mainstream industrialization and mature fabrication techniques of semiconductor manufacturing.

Acknowledgments

This work was supported by LifeLab Program of the 'Consorzio per la Ricerca Sanitaria' (CORIS) of the Veneto Region, Italy (DGR1017, 17 July 2018)

Disclosures

The authors declare no conflicts of interest.

See Supplement 1 for supporting content.

References

1. F. Capasso, "The future and promise of flat optics: a personal perspective," Nanophotonics **7**(6), 953–957 (2018).
2. F. S. Roux, "Geometric phase lens," J. Opt. Soc. Am. A **23**(2), 476–482 (2006).
3. P. Genevet, F. Capasso, F. Aieta, M. Khorasaninejad, and R. Devlin, "Recent advances in planar optics: from plasmonic to dielectric metasurfaces," Optica **4**(1), 139–152 (2017).
4. D. Lin, M. Meli, E. Poliakov, P. ST. Hilaire, S. Dhuey, C. Peroz, S. Cabrini, M. Brongersma, and M. Klug, "Optical metasurfaces for high angle steering at visible wavelengths," Sci. Rep. **7**(1), 2286 (2017).
5. A. Arbabi, R. M. Briggs, Y. Horie, M. Bagheri, and A. Faraon, "Efficient dielectric metasurface collimating lenses for mid-infrared quantum cascade lasers," Opt. Express **23**(26), 33310–33317 (2015).
6. B. Desiatov, N. Mazurski, Y. Fainman, and U. Levy, "Polarization selective beam shaping using nanoscale dielectric metasurfaces," Opt. Express **23**(17), 22611–22618 (2015).
7. M. Khorasaninejad and F. Capasso, "Metalenses: versatile multifunctional photonic components," Science **358**(6367), eaam8100 (2017).
8. W. T. Chen, A. Y. Zhu, J. Sisler, Z. Bharwani, and F. Capasso, "A broadband achromatic polarization-insensitive metalens consisting of anisotropic nanostructures," Nat. Commun. **10**(1), 355 (2019).
9. M. J. Padgett, "Orbital angular momentum 25 years on," Opt. Express **25**(10), 11265–11274 (2017).
10. R. C. Devlin, A. Ambrosio, D. Wintz, S. L. Oscurato, A. Y. Zhu, M. Khorasaninejad, J. Oh, P. Maddalena, and F. Capasso, "Spin-to-orbital angular momentum conversion in dielectric metasurfaces," Opt. Express **25**(1), 377–393 (2017).
11. R. C. Devlin, A. Ambrosio, N. A. Rubin, J. P. Balthasar Mueller, and F. Capasso, "Arbitrary spin-to-orbital angular momentum conversion of light," Science **358**(6365), 896–901 (2017).

Optics EXPRESS

12. B. Sephton, Y. W. Huang, A. Ambrosio, C. W. Qiu, A. Valles, T. Omatsu, F. Capasso, and A. Forbes, "Purity and efficiency of hybrid orbital angular momentum generating metasurfaces," J. Nanophotonics **14**(01), 1 (2020).
13. G. Ruffato, P. Capaldo, M. Massari, E. Mafakheri, and F. Romanato, "Total angular momentum sorting in the telecom infrared with silicon Pancharatnam-Berry transformation optics," Opt. Express **27**(11), 15750–15764 (2019).
14. H. Larocque, J. Gagnon-Bischoff, D. Mortimer, Y. Zhang, F. Bouchard, J. Upham, V. Grillo, R. W. Boyd, and E. Karimi, "Generalized optical angular momentum sorter and its application to high-dimensional quantum cryptography," Opt. Express **25**(17), 19832–19843 (2017).
15. S. Zheng, Y. Li, Q. Lin, X. Zeng, G. Zheng, Y. Cai, Z. Chen, S. Xu, and D. Fan, "Experimental realization to efficiently sort vector beams by polarization topological charge via Pancharatnam–Berry phase modulation," Photonics Res. **6**(5), 385–389 (2018).
16. S. M. Kamali, E. Arbabi, A. Arbabi, and A. Faraon, "A review of dielectric optical metasurfaces fo wavefront control," Nanophotonics **7**(6), 1041–1068 (2018).
17. Z. Bomzon, G. Biener, V. Kleiner, and E. Hasman, "Space-variant Pancharatnam–Berry phase optical elements with computer-generated subwavelength gratings," Opt. Lett. **27**(13), 1141–1143 (2002).
18. A. Niv, G. Biener, V. Kleiner, and E. Hasman, "Propagation-invariant vectorial Bessel beams obtained by use of quantized Pancharatnam-Berry phase optical elements," Opt. Lett. **29**(3), 238–240 (2004).
19. W. J. Hossack, A. M. Darling, and A. Dahdouh, "Coordinate transformations with multiple computer-generated optical elements," J. Mod. Opt. **34**(9), 1235–1250 (1987).
20. G. C. G. Berkhout, M. P. J. Lavery, J. Courtial, M. W. Beijersbergen, and M. J. Padgett, "Efficient sorting of orbital angular momentum states of light," Phys. Rev. Lett. **105**(15), 153601 (2010).
21. M. P. J. Lavery, D. J. Robertson, G. C. G. Berkhout, G. D. Love, M. J. Padgett, and J. Courtial, "Refractive elements for the measurements of the orbital angular momentum of a single photon," Opt. Express **20**(3), 2110–2115 (2012).
22. W. Li, K. S. Morgan, Y. Li, K. Miller, G. White, R. J. Watkins, and E. G. Johnson, "Rapidly tunable orbital angular momentum (OAM) system for higher order Bessel beams integrated in time (HOBBIT)," Opt. Express **27**(4), 3920–3934 (2019).
23. G. Ruffato, M. Massari, G. Parisi, and F. Romanato, "Test of mode division multiplexing and demultiplexing in free-space with diffractive transformation optics," Opt. Express **25**(7), 7859–7868 (2017).
24. G. Ruffato, M. Girardi, M. Massari, E. Mafakheri, B. Sephton, P. Capaldo, A. Forbes, and F. Romanato, "A compact diffractive sorter for high-resolution demultiplexing of orbital angular momentum beams," Sci. Rep. **8**(1), 10248 (2018).
25. G. Ruffato, M. Massari, M. Girardi, G. Parisi, M. Zontini, and F. Romanato, "Non-paraxial design and fabrication of a compact OAM sorter in the telecom infrared," Opt. Express **27**(17), 24123–24134 (2019).
26. S. Takashima, H. Kobayashi, and K. Iwashita, "Integer multiplier for the orbital angular momentum of light using a circular-sector transformation," Phys. Rev. A **100**(6), 063822 (2019).
27. G. Ruffato, M. Massari, and F. Romanato, "Multiplication and division of the orbital angular momentum of light with diffractive transformation optics," Light: Sci. Appl. **8**(1), 113 (2019).
28. A. Emoto, M. Nishi, M. Okada, S. Manabe, S. Matsui, N. Kawatsuki, and H. Ono, "Form birefringence in intrinsic birefringent media possessing a subwavelength structure," Appl. Opt. **49**(23), 4355–4361 (2010).
29. P. Capaldo, A. Mezzadrelli, A. Pozzato, G. Ruffato, M. Massari, and F. Romanato, "Nano-fabrication and characterization of silicon meta-surfaces provided with Pancharatnam-Berry effect," Opt. Mater. Express **9**(3), 1015–1032 (2019).
30. G. Ruffato, E. Rotunno, and V. Grillo, "A general framework for conformal transformations in electron optics," arXiv:2003.09635
31. M. G. Moharam, D. A. Pommet, E. B. Grann, and T. K. Gaylord, "Stable implementation of the rigorous coupled-wave analysis for surface-relief gratings: enhanced transmittance matrix approach," J. Opt. Soc. Am. A **12**(5), 1077–1086 (1995).
32. P. Lalanne, "Improved formulation of the coupled-wave method for two-dimensional gratings," J. Opt. Soc. Am. A **14**(7), 1592–1598 (1997).
33. H. Kikuta, Y. Ohira, H. Kubo, and K. Iwata, "Effective medium theory of two-dimensional subwavelength gratings in the non-quasi-static limit," J. Opt. Soc. Am. A **15**(6), 1577–1585 (1998).
34. M. Massari, G. Ruffato, M. Gintoli, F. Ricci, and F. Romanato, "Fabrication and characterization of high-quality spiral phase plates for optical applications," Appl. Opt. **54**(13), 4077–4083 (2015).
35. P. Pieranski, B. Yang, L.-J. Burtz, A. Camu, and F. Simonetti, "Generation of umbilics by magnets and flows," Liq. Cryst. **40**(12), 1593–1608 (2013).
36. G. Ruffato, E. Brasselet, M. Massari, and F. Romanato, "Electrically activated spin-controlled orbital angular momentum multiplexer," Appl. Phys. Lett. **113**(1), 011109 (2018).
37. E. Brasselet, "Tunable high-resolution macroscopic self-engineered geometric phase optical elements," Phys. Rev. Lett. **121**(3), 033901 (2018).